Nature-Inspired Cellular Structure Design for Electric Vehicle Battery Compartment: Application to Crashworthiness

Mohammed Mudassir [1] , **Faris Tarlochan** [1,2,*] **and Mahmoud Ashraf Mansour** [1]

1   Department of Mechanical and Industrial Engineering, College of Engineering, Qatar University, Doha 2713, Qatar; mh1204033@student.qu.edu.qa (M.M.); mm1201659@student.qu.edu.qa (M.A.M.)

2   Qatar Transportation and Traffic Safety Center (QTTSC), College of Engineering, Qatar University, Doha 2713, Qatar

*   Correspondence: faris.tarlochan@qu.edu.qa

Featured Application: The potential application of the work is in the area of the crashworthiness of electric vehicles. The study focuses on structural design to protect the vehicle battery in an event of a collision.

Abstract: This paper discusses the potential of using lightweight nature-inspired cellular structured designs as energy absorbers in crashworthiness applications for electric vehicles (EV). As EVs are becoming popular with their increased battery capacity, these lightweight cellular structures have regained research interest as they may increase mileage by reducing vehicle mass in addition to protecting the battery during collisions. In this paper, a novel lightweight cellular structure for EV battery protection and crashworthiness is designed and simulated. In designing the cellular structure, four different ways of applying the shell thickness have been considered that affects the collapse behavior and the crashworthiness. A numerical study was conducted on 45 samples with varying length, shell thicknesses, and thickness application methods. Four types of shell thickness application methods were investigated: Uniform thickness, strut-wall thickness, gradient thickness, and alternate thickness. Force-displacement curves, energy absorption, specific energy absorption, and collapse behaviors are some of the metrics used for evaluating the crashworthiness of the structures. Shell thickness is found to affect both the collapse behavior and energy absorption capabilities. Energy absorption results are similar to other studies on designed cellular structures. The highest performing cellular structure is reported to have a specific energy absorption of 35kJ/kg, which is comparable to cellular structures reported in the literature.

1. Introduction

By the year 2035, about two billion vehicles are expected to be used regularly around the world [1]. The majority of these vehicles will be gasoline-powered. With concerns about climate change and greenhouse gas (GHG) emissions, many governments are encouraging the use of electric vehicles (EVs). For instance, the Norwegian government incentivizes the use of EVs through different types of tax-cuts [2]. Such policies have made a positive impact, as Norway currently has the highest sale of EVs per capita with EVs being one-third of all cars sold in 2018 [3]. From sourcing the raw materials to manufacturing and maintenance, modern EVs produce just half of the GHG emissions over their lifetime compared to their average traditional counterparts [4]. Not only do EVs have lower GHG

emissions but they also have good performance making them lucrative purchases. Some of the high-end EV models that came out in 2019 can travel between 300 to 600 km per charge [5]. High-capacity rechargeable batteries and lightweight materials are two of the most important factors behind the success of modern EVs [6,7]. Unlike lead-acid based batteries in traditional cars that are mainly used for starting up the engines, batteries in EVs have more functions and require additional protection from tempering and accidents. Increasing the adoption of EVs everywhere means that there are more chances of EVs being involved in crashes, and these new types of batteries can pose different types of risks. Reports indicate that some lithium-ion batteries can spontaneously burst into flames while others can catch fire in accident causing fatalities [8,9]. Hence, more research and development are needed in improving protection systems for batteries in EVs as they come with new and unique challenges.

EVs can be of different types such as a plug-in hybrid electric vehicle (PHEV), range-extended electric vehicle (REEV), battery electric vehicle (BEV), and fuel cell electric vehicle (FCEV) [10–12]. The PHEVs and the REEVs have combustion engines along with electric motors, while the BEVs and FCEVs can run without a combustion engine. Based on the load-carrying capacity, the required speed, and the driving conditions among other factors, these vehicles can have different battery capacities and other design parameters. For a long time, the automobile depended on lead-acid based batteries. However, these batteries are too heavy to be used in powering long-range consumer vehicles. Today, some EVs use nickel-metal hydride (Ni-MH) based batteries, while most other EVs use lithium-ion based batteries as the de facto power source [13]. Typically, the batteries are packed together into modules [6]. Power consumption for typical consumer EVs can vary between 11 to 15 kWh/100 km [14]. Batteries in EVs are placed either at the center of the car or at the rear as illustrated in Figure 1 [15]. The battery modules are protected through multi-layer casings (Figure 2). Typically, there is an aluminum underbody protection, aluminum extrusion ring for crash absorption, steel tub with flanges and inner walls for the battery modules, and a steel housing cover [16]. Battery casings are designed taking into account the different challenges related to the safety, thermal runway, electric discharge, and mechanical vibrations [17,18]. The focus of this study is limited to the aluminum crash structure as shown in Figure 2. The aim is to replace this crash structure with cellular structures. Most automobiles instead use tubular structures for crashworthiness [19–23]. With EVs becoming more popular, lightweight metal cellular structures are regaining interest as promising materials for the crashworthiness of the battery housing.
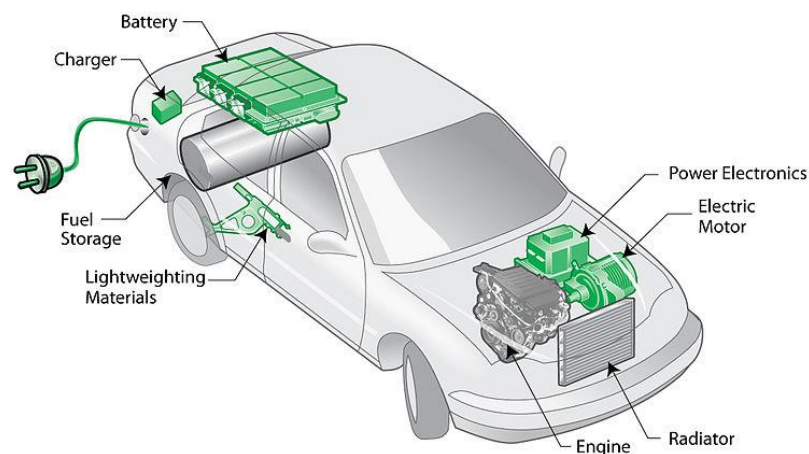

Figure 1. Illustration of an electric vehicle with the battery installed at the rear [15].
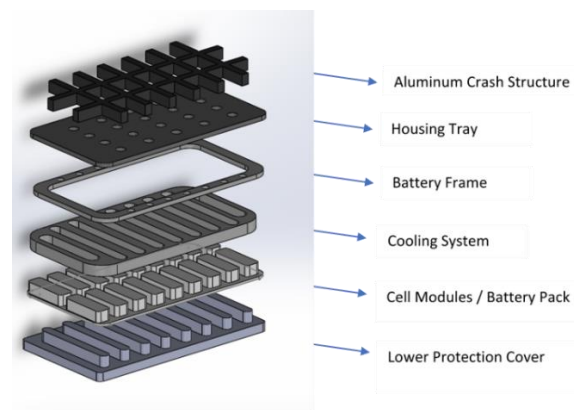
Figure 2. Illustration of a multilayered housing for battery casing.

Metallic cellular structured materials are basically material with pores and have a density less than the material bulk density, depending on the porosity levels [24]. Examples of such materials are metallic foams or metallic honeycomb-like structures. Such cellular structured materials when they collapse under axial loading allow the structure to compress without significant transversal deformation. The influence of cell microstructure on the behavior is due to the fact that the deformation mechanism of the material at cell level is governed by bending and stretching of the cell wall followed by buckling at a post-yield stage [25]. This along with the plateau stress behavior (near constant deformation resistance) makes metallic cellular structures attractive for crashworthiness applications [24–31], as depicted in Figure 3.
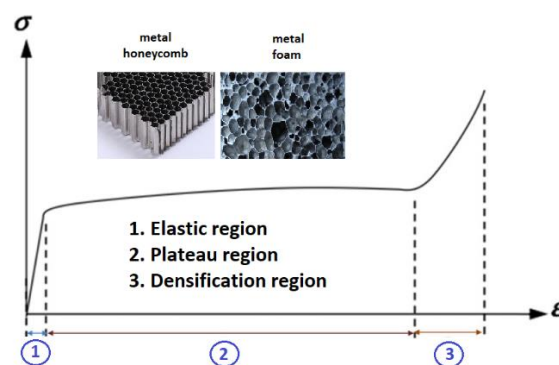

Figure 3. Typical stress-strain characteristics for cellular structures such as foams and honeycombs.

Metallic foam cellular structures have long been used for energy absorption. However, due to inconsistent mechanical properties that arise from the traditional methods of manufacturing, they cannot be used reliably [25,32]. This is because the stabilization mechanism of metallic foams is still not fully understood, and is mainly due to the mechanisms of metal melting and thermal decomposition of the blowing agent [32–35]. The approach taken here is to design novel cellular structures inspired by nature and at the same time can be produced from additive manufacturing to maintain consistency in material properties [36–38], unlike the traditional means of producing metal foams as discussed previously. Nature offers many excellent examples of structures with low density, high strength, and high energy absorption capacities. One of these is the honeycomb [39,40]. The cellular structure geometry for this study is inspired by the honeycomb structure. Furthermore, with additive manufacturing becoming widely available, fabrication of complex cellular structures is no longer a challenging feat [36–38]. The design of the inspiration is shown in Figure 4. Following the trend, in this paper, we propose novel cellular lightweight structures design for the electric vehicle battery housing for crashworthiness. These cellular structures are designed and modeled using the finite element software. The focus of this

paper will be on metallic cellular structures for weight reduction purposes, in particular aluminum based cellular structures for their lightweight.
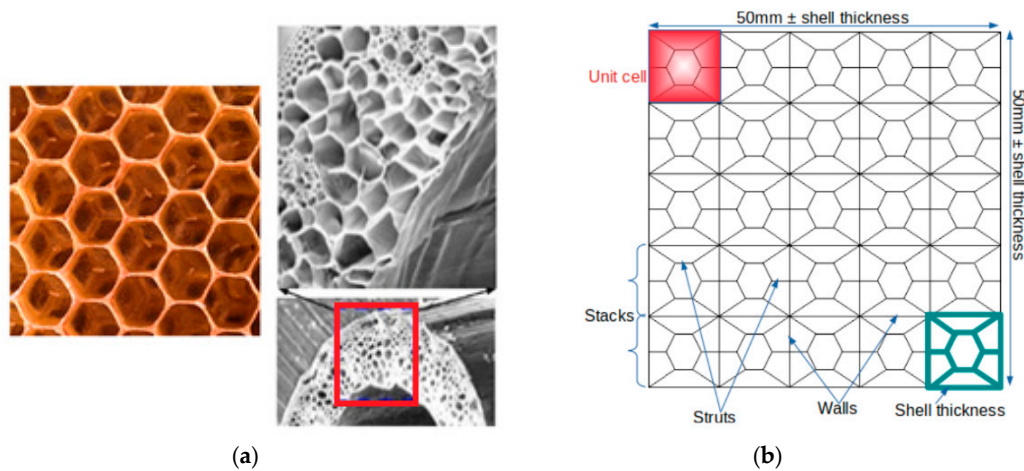

Figure 4. (**a**) Honeycomb design in nature, (**b**) nature-inspired cellular structure design for this study. The novelty is through the addition of walls and struts to the honeycomb design.

2. Performance Metrics, Geometry, and Material Properties

2.1. Performance Metrics

Several metrics exist for evaluating the performance of cellular structures. In this paper, we will focus on peak force, mean crushing force, energy absorption, and specific energy absorption. *Peak force*—initiating the plastic deformation of the cellular structure requires a large starting load that often shows up as a peak on the force-displace diagram. The peak force is denoted by F_P. A low initial peak force is desirable so that the damage to the battery module would be minimized. *Mean force*—after the peak force, the cellular structure continues to crumple until it reaches the densification zone. Densification usually occurs around a 60% strain. This means force is denoted by F_μ, and it is calculated by taking the average of the forces from the peak force until the densification point. *Energy absorption*—E_A, is calculated as the area under the force-displacement curve from the start of the crushing until it reaches the start of the densification zone marked by the steep rise of the force-displacement curve. Cellular structures with high-energy absorption capacity are desirable. *Specific energy absorption*—E_{SEA}, is obtained by dividing the E_A by the crushed mass, M_C. It allows us to compare different cellular structures with different masses that can have varying E_A capacities.

2.2. Cellular Structure Geometry

Figure 4 shows the geometry of the cellular structure. The unit cell is a hexagon connected to a 10×10 mm square from its six corners. The sides of the square are considered walls whereas the hexagon and the lines extending from its corners are considered struts. The cellular structure is made from stacks of unit cells. The volume of the cellular structure is $50 \times 50 \times L$ mm. The length (L) is increased from 50 to 150 mm (increments of 50 mm) for studying the effects of length scaling. The struts, walls, and stacks are assigned thicknesses in four different ways as discussed below.

The uniform shell thickness (UT) is shown in Figure 5 where the struts and the walls have the same shell thickness. There is no variation in shell thickness in different stacks or elsewhere for UT. In the strut-wall shell thickness (SWT) type, the struts and the walls have varying shell thickness assignments. As shown in Figure 6, the walls have a thickness of T_2 while the struts have a thickness of T_1 different from the former. Figure 7 shows the alternating shell thickness (AT) type where the struts and walls alternate between two thicknesses T_1 and T_2. Starting with the left-most unit cell at the bottom stack, the struts are assigned a thickness of T_1. The next group of struts on its right is

assigned T_2, etc. For the wall thickness, the whole cellular structure is considered instead of the unit cell. The bottom wall of the bottom stack is assigned T_1 and the top wall of the bottom stack is assigned T_2. This pattern is repeated for all the horizontal walls. The first vertical wall of the first column-stack is assigned T_1 and the second vertical wall of the first column stack is assigned T_2, etc. The gradient shell thickness (GT) type has an incremental shell thickness based on the stacking levels. As depicted in Figure 8 the lowest stack has a thickness of T_1 and it increases as we move up along the stacks until we reach the top-most stack, which has a thickness of T_2.
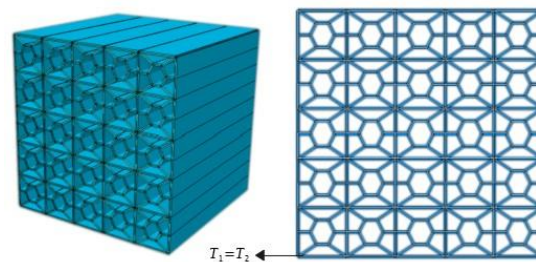
Figure 5. Uniform thickness with an isometric view (**left**) and front view (**right**). Thickness assignments to the walls (T_2) and the struts (T_1) are equal.
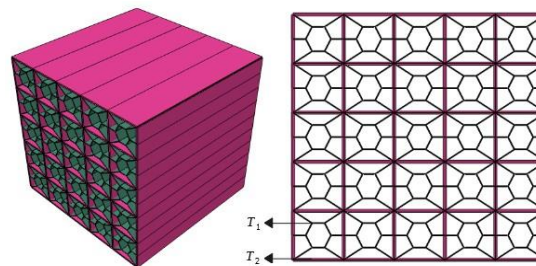
Figure 6. Strut-wall thickness with an isometric view (**left**) and front view (**right**). Thickness assignments to the walls (T_2) and the struts (T_1) are different.
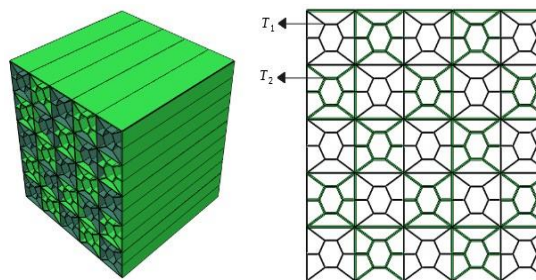
Figure 7. Alternating thickness with an isometric view (**left**) and front view (**right**). Thickness assignments indicate the maximum (T_2) and minimum (T_1) values.
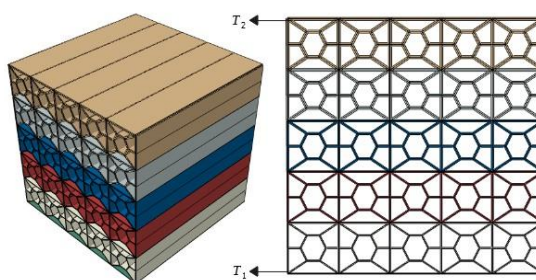
Figure 8. Gradient thickness with an isometric view (**left**) and front view (**right**). Thickness assignments to the stacks indicate the maximum (T_2) and minimum (T_1) values at that level.

Table 1 summarizes the geometric parameters we have discussed thus far. It also specifies the values that we have considered for these parameters. There are four geometric parameters: Strut thickness, wall thickness, gradient thickness, and length. The struts and walls can have either 0.2, 0.4, or 0.6 mm thickness for UT, SWT, and AT. Whereas the stacks are assigned a gradient thickness for GT which is calculated by $(T_2 - T_1)/L$. For each of these geometric types, the length can be 50, 100, or 150 mm. These all together result in 45 simulations as indicated in Table 2.

Table 1. Geometric parameters.

Parameters	Values
Strut thickness	0.2, 0.4, or 0.6 mm
Wall thickness	0.2, 0.4, or 0.6 mm
Gradient(*s*)	$(T_2 - T_1)/L$
Length(*L*)	50, 100, or 150 mm

Table 2. Assortment and number of simulations.

Type	Assortment	Simulations
UT	Struts = T_1, Walls = T_2, Length = L	9
SWT	Struts = T_1, Walls = T_2, Length = L	18
AT	(Struts, Walls)i = T_1, (Struts, Walls)i+1 = T_2, Length = L	9
GT	Stacks = $T_1 \rightarrow T_2$ with s increments, Length = L	9

2.3. Material Properties

The cellular structure material is modeled by Aluminum AA2024 Johnson-Cook material properties as shown in Table 3 [41,42]. The Johnson-Cook material equation is given by (1), where parameters *A*, *B*, *C*, and *n* are empirical constants, ϵ is the plastic strain, σ is the material flow stress, $\dot{\epsilon}$ is the strain rate, and $\dot{\epsilon}_0$ is the reference strain rate. In this study, the temperature factor was not considered as it is assumed that the change of temperature due to plastic deformation is negligible to cause changes in material behavior [43].

$$\sigma = [A + B\epsilon^n]\left[1 + C\ln\left(\frac{\dot{\epsilon}}{\dot{\epsilon}_0}\right)\right] \tag{1}$$

Table 3. Aluminum AA2024 Johnson-Cook Material Properties [41,42].

Parameters	Values
E	73.1 GPa
ν	0.33
A	276 MPa
B	700 MPa
C	0.0001726
n	0.421
m	1.37
Tm	502 °C
Tt	413 °C
$\dot{\epsilon}_0$	1 s^{-1}
ρ	2780 kg/m^3

3. Finite Element Model

The finite element model is set up using a commercial nonlinear finite element code. A dynamic explicit analysis is used for simulating the crushing of the cellular structure. The model assembly consists of a planar rigid striker, a planar rigid base, and a 3D deformable shell cellular structure as shown in Figure 9a. The striker is assigned an inertial mass of 275 kg with a velocity of 15 m/s [22,44].

During head-on collisions, the two frontal tubes are expected to absorb less than 50% of the mass kinetic energy of the vehicle to protect the passengers [44,45]. Since batteries are either located at the back, the sides, or the center of the vehicle, they are not a primary concern during a frontal collision. However, assuming that the cellular structures need to absorb an equivalent amount of kinetic energy during a side or a rear impact, the inertial mass is set at 275 kg, which is 25% of the mass of a compact electric vehicle of 1100 kg [22]. While the striker is free to move along [±Y], it cannot rotate or translate along any other axes. The base is fixed and assigned a tie-constrain with the cellular structure. The cellular structure was meshed using the S4R shell continuum element with a mesh size of 0.8. The mesh size is selected after a mesh sensitivity analysis as shown in Table 4. F_P, F_μ, E_A, and E_{SEA} all start converging at a mesh size of 0.8 within a reasonable computation time. The general model (boundary condition, material model, and constraints) is validated using the model described by [23]. We managed to obtain good accuracy. After which, we used this model and replaced the tubular geometry with our cellular structure geometry. The material model used in both cases are Johnson-Cook which is well established in the literature and is commonly used with aluminum alloy materials. To validate further our FE model used in this paper, a cellular structure geometry from the literature [46], as shown in Figure 9b, and Johnson-Cook AA3003 material properties [47] was used. We simulated the work in [46] using the FE model presented in this paper with slight changes to the material properties [47] and inertia values to meet the requirements of [46]. The specific energy absorption values reported in [46] are compared to our FE model simulations as depicted in Table 5. It is demonstrated that the error between [46] and our FE approach is small.
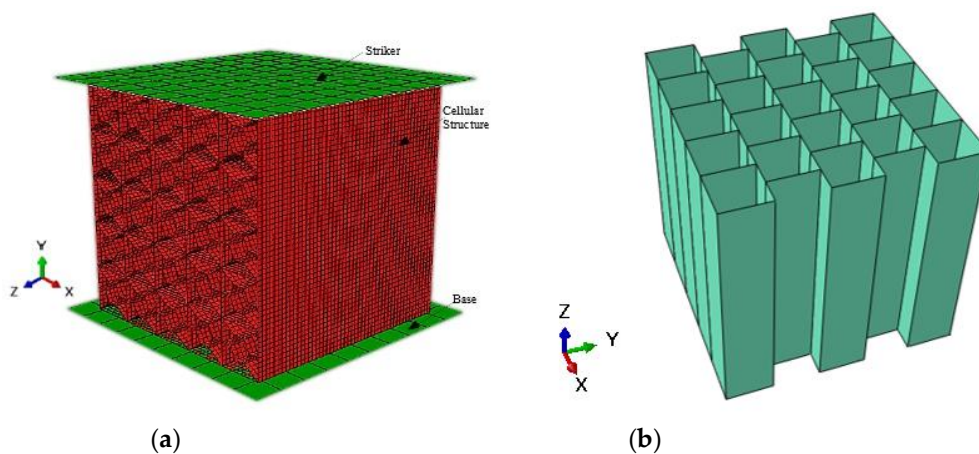

(a)　　　　　　　　　　　　　　　　　　　　　　　　　(b)

Figure 9. (**a**) The finite element model consists of a rigid striker that can translate along [-Y] with a specified velocity, a deformable cellular structure tied to a base, and a rigid base that is encastre (**b**) geometry used for validation purposes, maintaining the same model in (**a**).

Table 4. Mesh convergence study.

Mesh Size	F_P [N]	F_μ [N]	E_A [kJ]	E_{SEA} [kJ/kg]	CPU Time [s]
0.6	12.5	7.7	0.23	8.6	11,220
0.8	13	7.7	0.23	8.7	3050
1	14.5	8	0.24	9	2660
1.2	18.7	9	0.27	10	1200
1.4	19	9	0.27	10	700

Table 5. Comparison of E_{SEA} between our finite element (FE) model study vs. the reported ones in [46].

l/t	Reported SEA [46], (MJ/m^3)	Simulated Results, (MJ/m^3)	|Error| %
250	0.30982	0.31753	2.49
125	0.77395	0.75346	2.65
83.3	1.38624	1.33263	3.87
62.5	2.11718	2.03104	4.07

4. Discussion

The results in the following sub-sections will discuss each design configuration in terms of the force-displacement behaviors, deformation modes, and evaluation of the performance metrics. The force-displacement diagrams for all the 45 samples (Table 2) is attached in the Appendix A of this paper for the ease of comparison.

4.1. Uniform Thickness (UT) Design

Table 6 and Figure 10 summarize the results on the performance metrics for the cellular structure with the UT design configuration. To understand the meaning of these findings, Figures 11–13 will be used.

Table 6. Uniform thickness (UT) design factors and performance metrics.

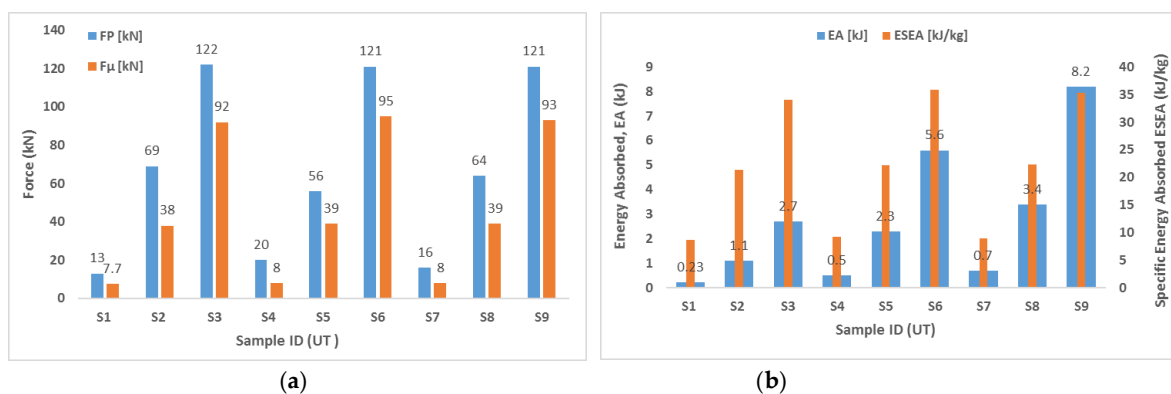| ID	Type	T_1	T_2	L	F_P	F_μ	E_A	E_{SEA}
		[mm]	[mm]	[mm]	[kN]	[kN]	[kJ]	[kJ/kg]
S1		0.2	0.2	50	13	7.7	0.23	8.7
S2	UT (50 × 50 × 50)	0.4	0.4	50	69	38	1.1	21.4
S3		0.6	0.6	50	122	92	2.7	34
S4		0.2	0.2	100	20	8	0.5	9.2
S5	UT (50 × 50 × 100)	0.4	0.4	100	56	39	2.3	22.2
S6		0.6	0.6	100	121	95	5.6	35.8
S7		0.2	0.2	150	16	8	0.7	8.9
S8	UT (50 × 50 × 150)	0.4	0.4	150	64	39	3.4	22.3
S9		0.6	0.6	150	121	93	8.2	35.3

Figure 10. Performance metrics for the UT design. (**a**) Peak and mean forces, (**b**) energy absorption metrics.
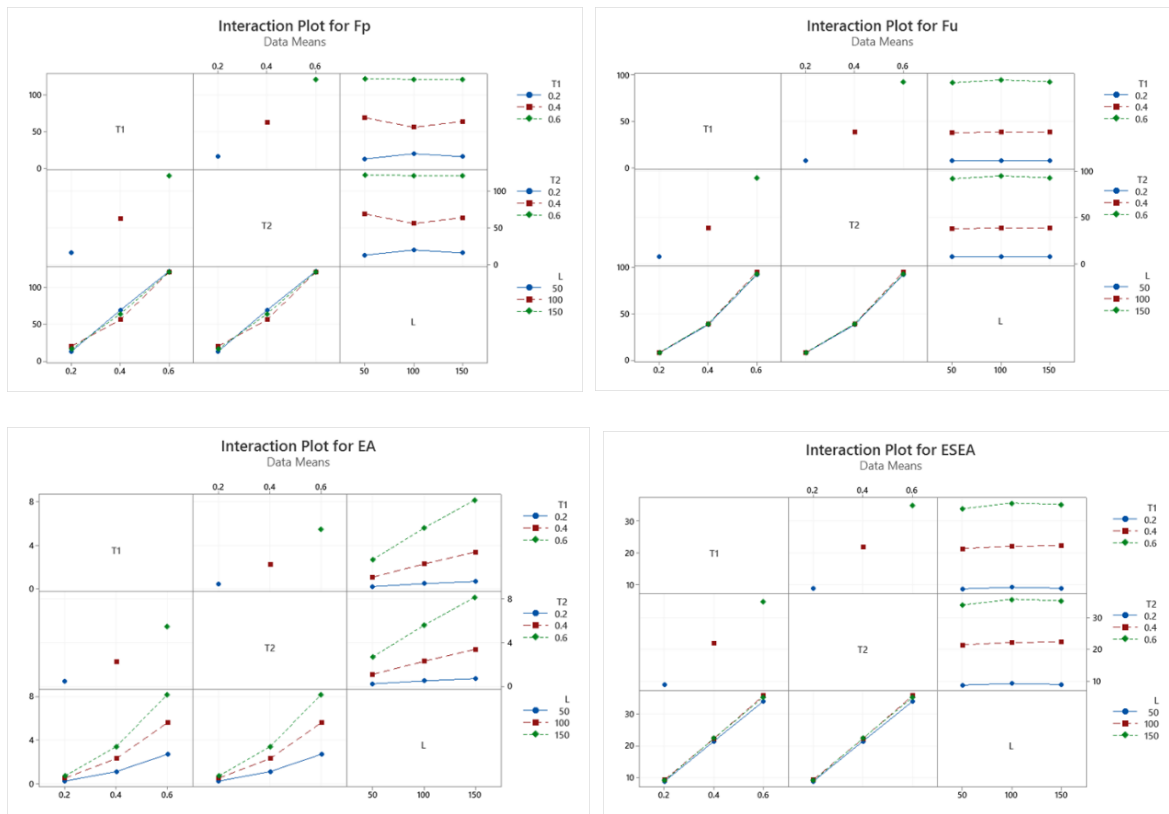
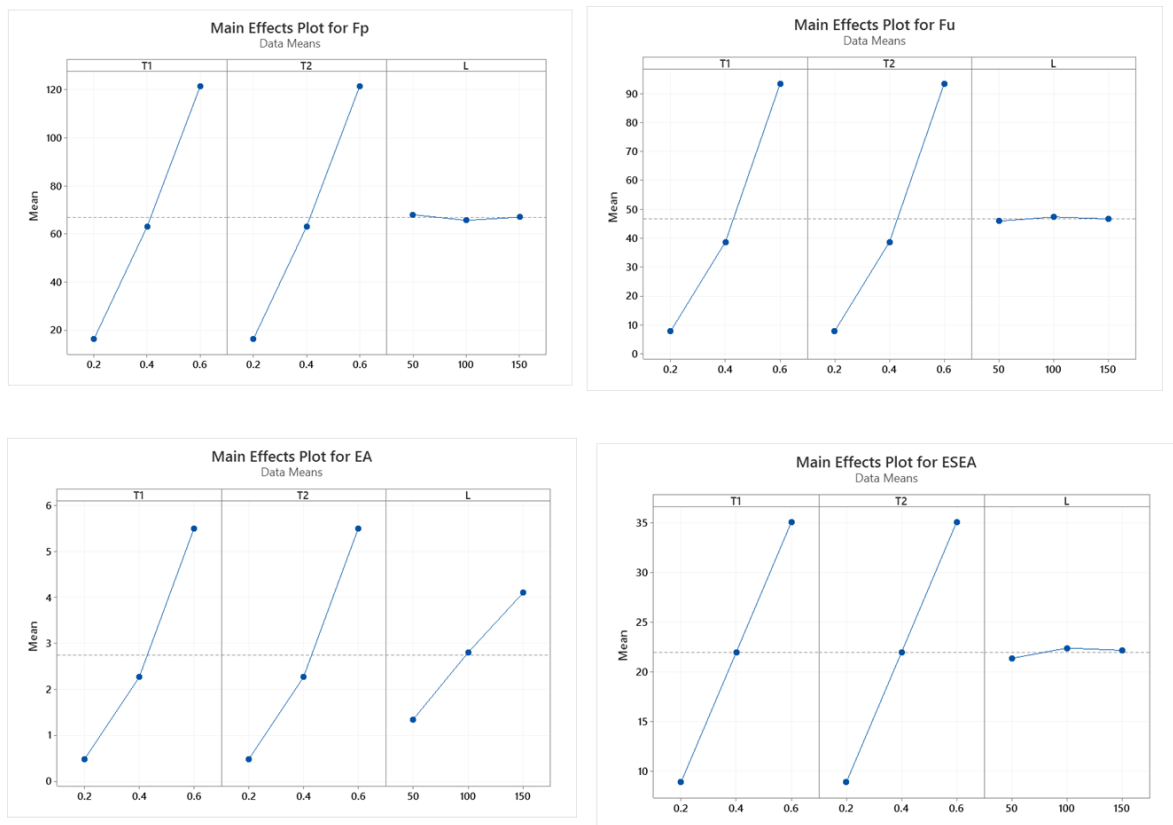**Figure 11.** Interaction plots between design parameters and performance metrics for the UT design.

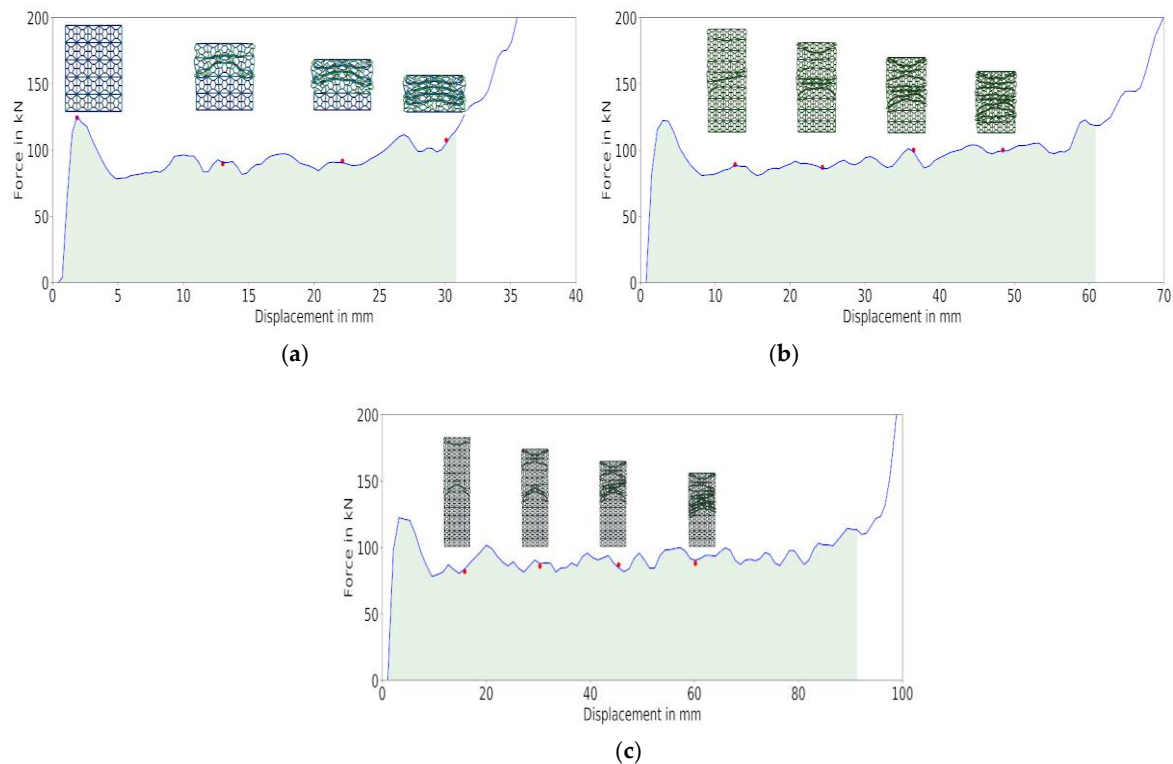**Figure 12.** Mean effect plots for each performance metric with respect to the design factors.

Figure 13. Example of force-displacement and deformation modes for (**a**) *L* = 50 mm, (**b**) *L* = 100 mm, (**c**) *L* = 150 mm. The shaded area indicates the energy absorbed before densification.

To better understand the effect of design factors (thicknesses and length) on the responses (performance metrics) interaction plots are used. From Figure 11, it is evident that there are no interaction effects between these design factors. Meaning, these design factors are independent of each other. This is because on interaction plots, parallel lines indicate that there is no interaction effect while different slopes (positive versus negative slopes) suggest that one might be present. This finding allows us to safely interpret the *mean plots* for each response based on the design factors as shown in Figure 12. From Figure 12, it is evident that (i) the peak and mean forces increase as the thickness T_1 and T_2 increases. However, these forces are not affected by the length of the structure. The same applies to the specific energy absorption (E_{SEA}) and (ii) the energy absorption (E_A) is affected by all three factors, including length. This is obvious since there is more deformation distance before densification is reached. From these performance metrics, the mean force and E_{SEA} are most crucial to be looked at. Hence, it can be concluded that the length of the structure is not a crucial factor to be considered. This will have an implication on the design space and manufacturing requirements. Figure 13 depicts a typical force-displacement graph along with the deformation mode for these structures. These diagrams are for $T_1 = T_2 = 0.6$ mm. It can be seen that the deformation mode is stable indicating good crash absorber characteristics. This figure also depicts that the average force and peak force is almost similar for all lengths, indicating once again that the length is not a crucial factor.

4.2. Strut-Wall Thickness (SWT) Design

Table 7 and Figure 14 summarize the results on the performance metrics for the cellular structure with a SWT design configuration. To understand the meaning of these findings, Figures 15–17 will be used.

From Figure 15 (*interaction plots*), it is evident that there are no interaction effects between the design factors and performance metrics. Meaning, these design factors are independent of each other. As stated earlier in the interaction plots if these lines are parallel it indicates that there are no interaction effects. This finding allows us to safely interpret the *mean plots* for each response based on the design

factors as shown in Figure 17. From Figure 17, it is evident that the change in peak force is mainly contributed by T_2 *(outer wall thickness)*. Once the peak force is achieved, the progressive deformation mean force is dominated by both T_1 and T_2. These forces are not affected by the length of the structure. The energy absorption is affected by all three factors, including length. This is obvious since there is more deformation distance before densification is reached. From these performance metrics, the mean force and E_{SEA} are most crucial to be looked at. Hence, it can be concluded that the length of the structure is not a crucial factor to be considered. This will have an implication on the design space and manufacturing requirements. Figure 16 depicts a typical force-displacement graph along with the deformation mode for these structures. It can be seen that the deformation mode is stable indicating good crash absorber characteristics. This figure also depicts that the average force and peak force is almost similar for all lengths, indicating once again that the length is not a crucial factor.

Table 7. SWT design factors and performance metrics.

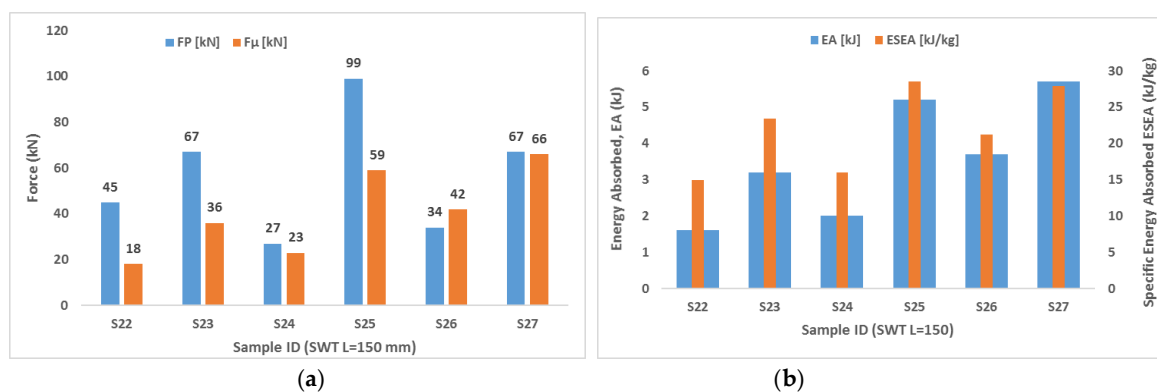| ID	Type	*T1* [mm]	*T2* [mm]	*L* [mm]	*FP* [kN]	*Fµ* [kN]	*EA* [kJ]	*ESEA* [kJ/kg]
S10		0.2	0.4	50	45	18	0.5	14.9
S11		0.2	0.6	50	71	36	1	22.5
S12	SWT (50 × 50 × 50)	0.4	0.2	50	24	23	0.7	15.5
S13		0.4	0.6	50	101	58	1.7	27.3
S14		0.6	0.2	50	35	42	1.2	21
S15		0.6	0.4	50	84	67	2	29
S16		0.2	0.4	100	47	18	1.1	15
S17		0.2	0.6	100	74	37	2.2	24
S18	SWT (50 × 50 × 100)	0.4	0.2	100	24	23	1.3	15.6
S19		0.4	0.6	100	98	59	3.5	28.2
S20		0.6	0.2	100	35	42	2.5	20.9
S21		0.6	0.4	100	76	67	3.9	28.8
S22		0.2	0.4	150	45	18	1.6	15
S23		0.2	0.6	150	67	36	3.2	23.4
S24	SWT (50 × 50 × 150)	0.4	0.2	150	27	23	2	16
S25		0.4	0.6	150	99	59	5.2	28.5
S26		0.6	0.2	150	34	42	3.7	21.2
S27		0.6	0.4	150	67	66	5.7	27.9

Figure 14. Performance metrics for the SWT design. (**a**) Peak and mean forces, (**b**) energy absorption.
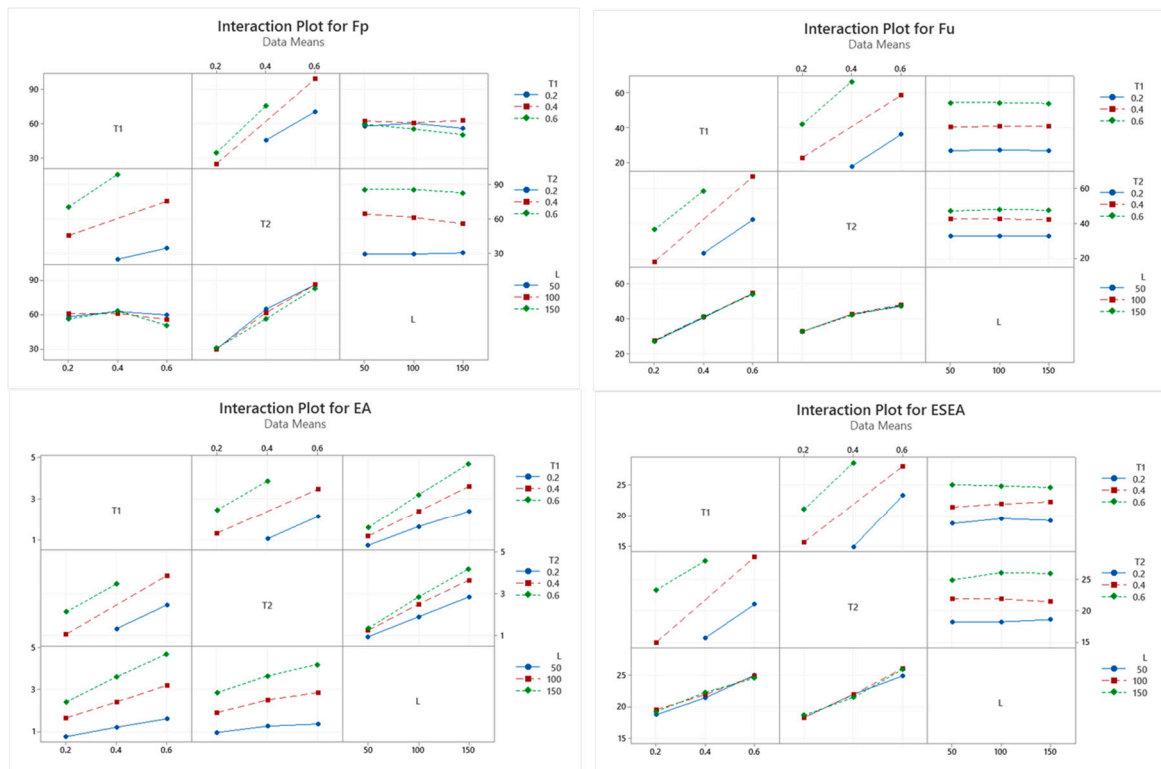
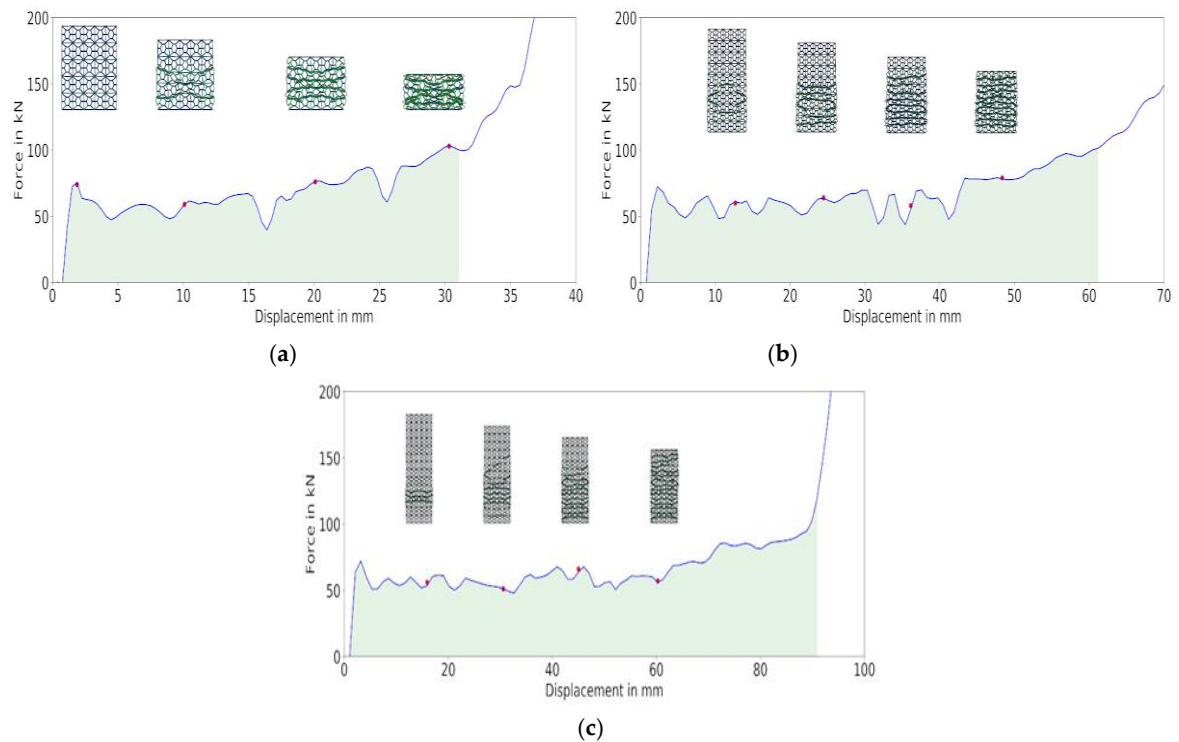**Figure 15.** Interaction plots between design parameters and performance metrics for the SWT design.

Figure 16. Example of force-displacement and deformation modes for (**a**) $L = 50$ mm, (**b**) $L = 100$ mm, (**c**) $L = 150$ mm. The shaded area indicates the energy absorbed before densification.
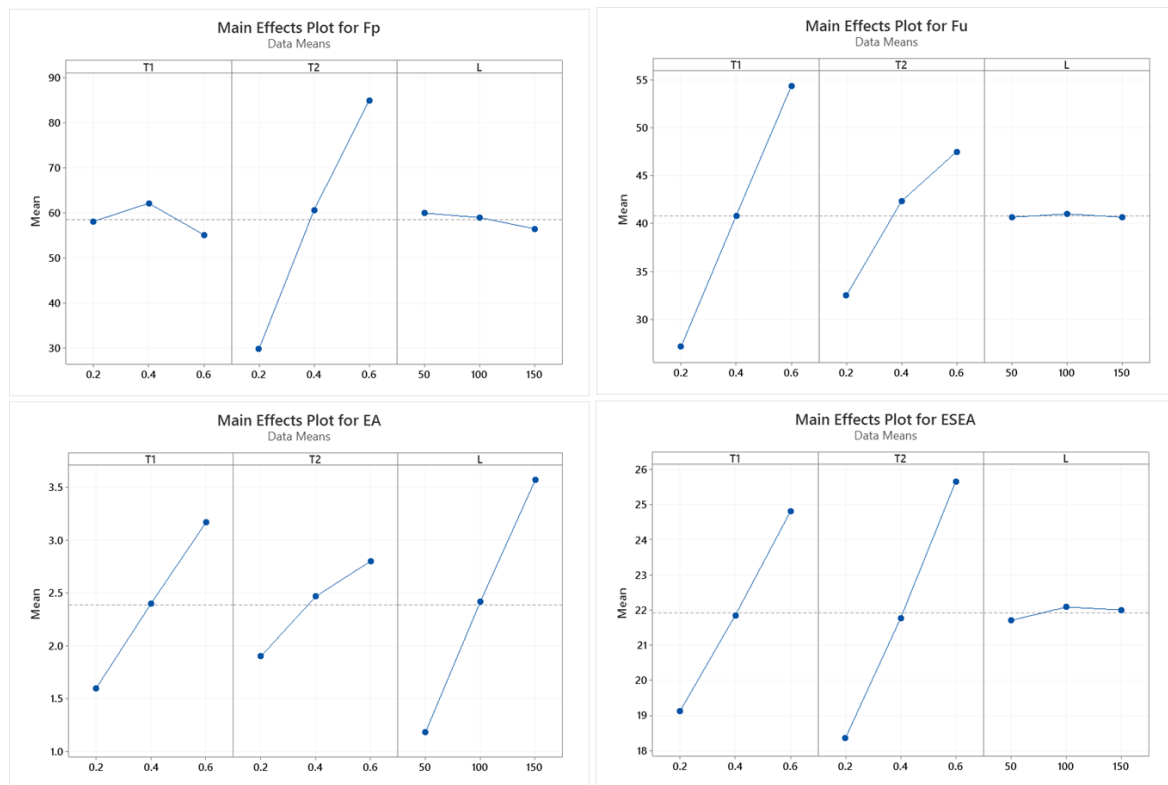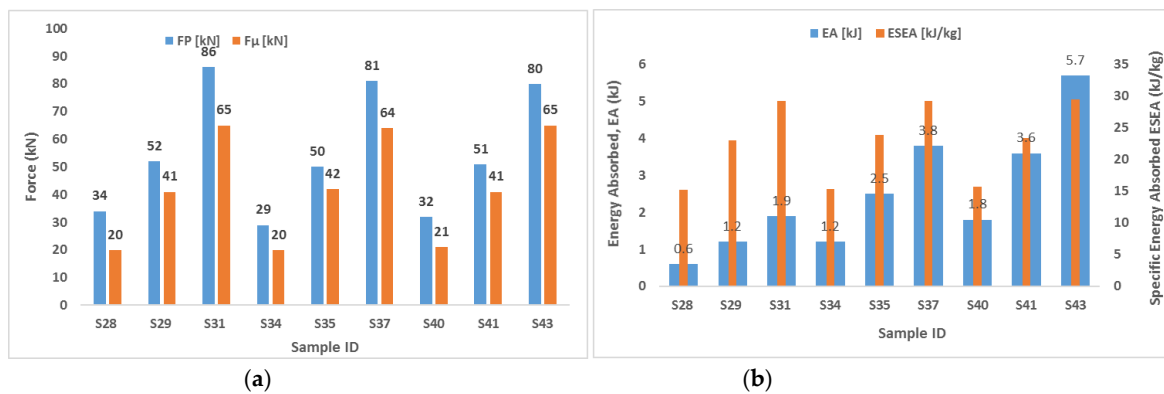
Figure 17. Mean effect plots for each performance metric with respect to the design factors.

4.3. Alternating Thickness (AT) Design

Table 8 and Figure 18 summarize the results on the performance metrics for the cellular structure with a SWT design configuration. To understand the meaning of these findings, Figures 19–21 will be used.

From Figure 19, it is evident that there are no interaction effects between these design factors. This finding allows us to safely interpret the *mean plots* for each response based on the design factors as shown in Figure 20. From Figure 20, it is evident that (i) the peak and mean forces increase as the thickness T_1 and T_2 increases. However, these forces are not affected by the length of the structure. The same applies for the specific energy absorption (E_{SEA}) and (ii) the energy absorption is affected by all three factors, including length. This is obvious since there is more deformation distance before densification is reached. From these performance metrics, the mean force and E_{SEA} are most crucial to be looked at. Hence, it can be concluded that the length of the structure is not a crucial factor to be considered. This will have an implication on the design space and manufacturing requirements. Figure 21 depicts a typical force displacement graph along with the deformation mode for these structures. It can be seen that the deformation mode and response are also stable indicating good crash absorber characteristics. However, unlike the UT and SWT designs, from Figure 21, it is evident that the deformation modes not only are in a progressive manner, there is also a slight global buckling taking place in the structures with lengths 100 and 150 mm, respectively. This indicates that the design variables T_1 and T_2 are producing a structure with less stiffness when compared to UT and SWT.

Table 8. Alternating thickness (AT) design factors and performance metrics.

ID	Type	T1	T2	L	FP	Fμ	EA	ESEA
		[mm]	[mm]	[mm]	[kN]	[kN]	[kJ]	[kJ/kg]
S28		0.2	0.4	50	34	20	0.6	15.2
S29	AT (50 × 50 × 50)	0.2	0.6	50	52	41	1.2	23
S31		0.4	0.6	50	86	65	1.9	29.2
S34		0.2	0.4	100	29	20	1.2	15.4
S35	AT (50 × 50 × 100)	0.2	0.6	100	50	42	2.5	23.9
S37		0.4	0.6	100	81	64	3.8	29.2
S40		0.2	0.4	150	32	21	1.8	15.7
S41	AT (50 × 50 × 150)	0.2	0.6	150	51	41	3.6	23.4
S43		0.4	0.6	150	80	65	5.7	29.5

(a)　　　　　　　　　　　　　　　　　　　　(b)

Figure 18. Performance metrics for the SWT design. (**a**) Peak and mean forces, (**b**) energy absorption.

Figure 19. Interaction plots between design parameters and performance metrics for the AT design.
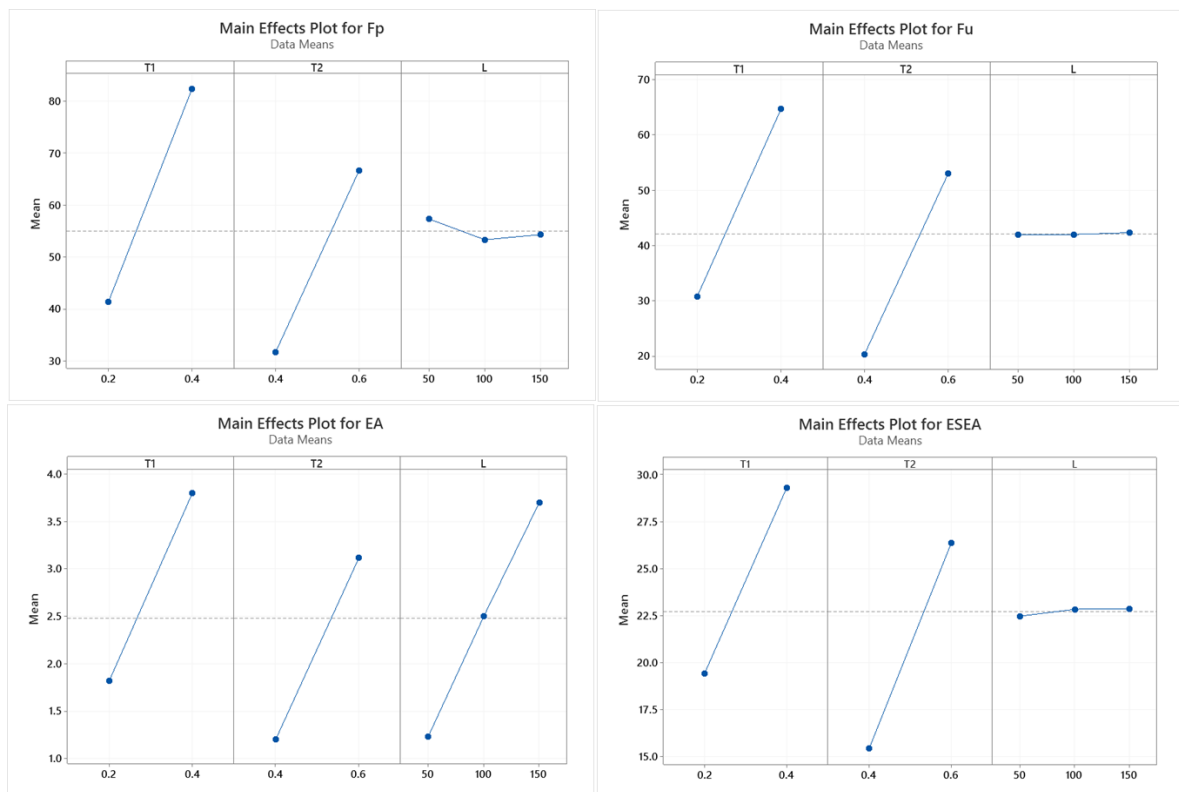
Figure 20. Mean effect plots for each performance metric with respect to the design factors.
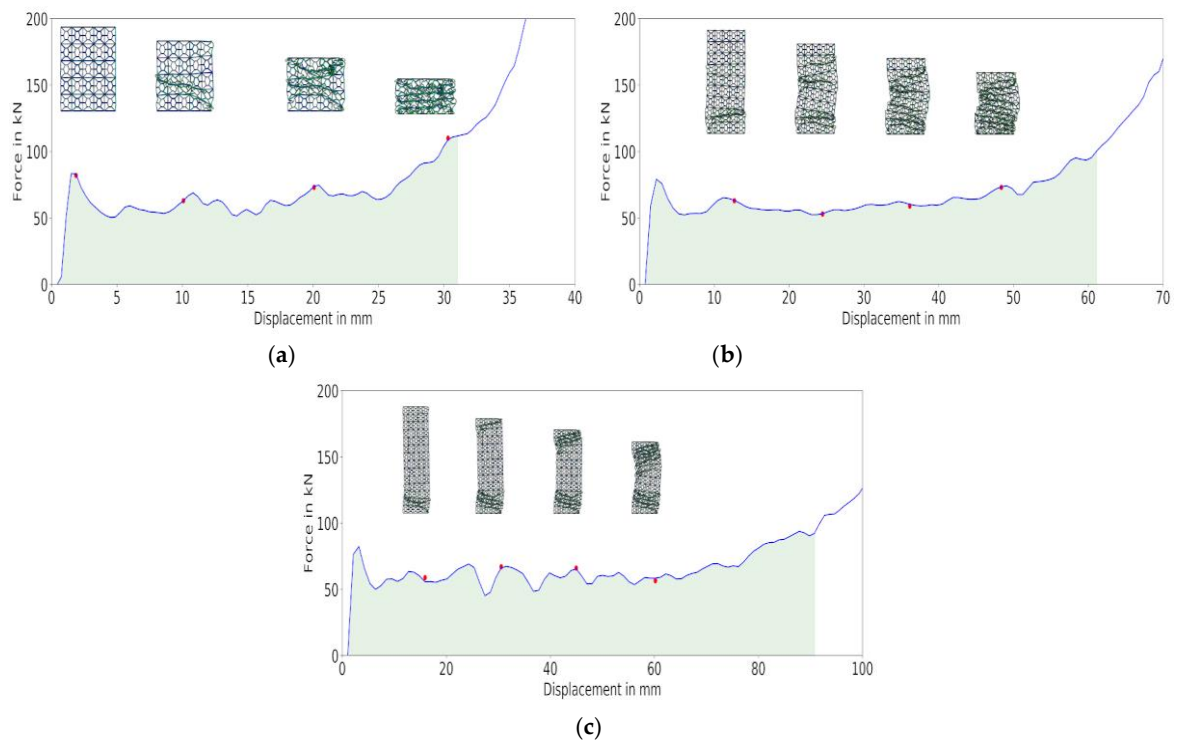

Figure 21. Example of force-displacement and deformation modes for (**a**) $L = 50$ mm, (**b**) $L = 100$ mm, (**c**) $L = 150$ mm. The shaded area indicates the energy absorbed before densification.

4.4. Grading Thickness (GT) Design

Table 9 and Figure 22 summarize the results on the performance metrics for the cellular structure with a SWT design configuration. To understand the meaning of these findings, Figures 23–25 will be used.

From Table 9 and Figures 22–24, it is evident that the gradient has an insignificant impact on the performance metrics. The main contributor to the performance metrics is the thickness and length. Unlike the previous three designs, the length of the structure significantly affects gradient design. Figure 25 depicts the force-displacement diagram. It shows that the deformation modes are in a progressive and stable manner.

Based on E_{SEA}, the cellular structures with the highest specific energy absorption from each group (UT, SWT, AT, GT) were selected. Sample S3 and its corresponding samples S6 and S9 with 100 and 150 mm, respectively had the highest E_{SEA} among all specimen with 35 kJ/kg (S9), which is comparable to the results found by [29,30]. Sample S15 was the highest among the SWT type with 28.8 kJ/kg and its corresponding samples of 100 and 150 mm length are S21 and S27, respectively. The best E_{SEA} for the AT type was sample S31 with 29 kJ/kg and the corresponding S37 and S48 of 100 and 150 mm, respectively. The best E_{SEA} for the GT type was sample S48 with 29.6 kJ/kg and a gradient of 0.004. It is apparent that the UT configuration design will be the most suitable candidate as the crash energy absorber to replace existing designs in EV. The E_{SEA} value obtained for the UT design (35 kJ/kg) is much higher than those reported for metallic aluminum forms (less than 10 kJ/kg) [31], however comparatively close with aluminum honeycomb structures (less than 45 kJ/kg) [31].

Table 9. Grading thickness (GT) design factors and performance metrics.

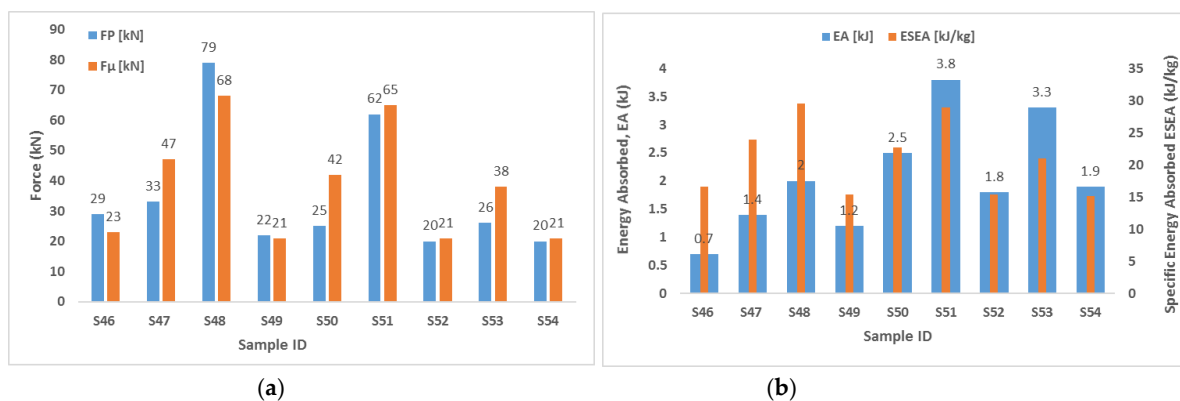| ID	Type	T1	T2	L	Gradient	FP	Fµ	EA	ESEA
		[mm]	[mm]	[mm]		[kN]	[kN]	[kJ]	[kJ/kg]
S46		0.2	0.4	50	0.004	29	23	0.7	16.6
S47	GT (50 × 50 × 50)	0.2	0.6	50	0.008	33	47	1.4	23.9
S48		0.4	0.6	50	0.004	79	68	2	29.6
S49		0.2	0.4	100	0.002	22	21	1.2	15.4
S50	GT (50 × 50 × 100)	0.2	0.6	100	0.004	25	42	2.5	22.7
S51		0.4	0.6	100	0.002	62	65	3.8	28.9
S52		0.2	0.4	150	0.001	20	21	1.8	15.4
S53	GT (50 × 50 × 150)	0.2	0.6	150	0.003	26	38	3.3	21
S54		0.4	0.6	150	0.001	20	21	1.9	15.1

Figure 22. Performance metrics for the SWT design. (**a**) Peak and mean forces, (**b**) energy absorption.
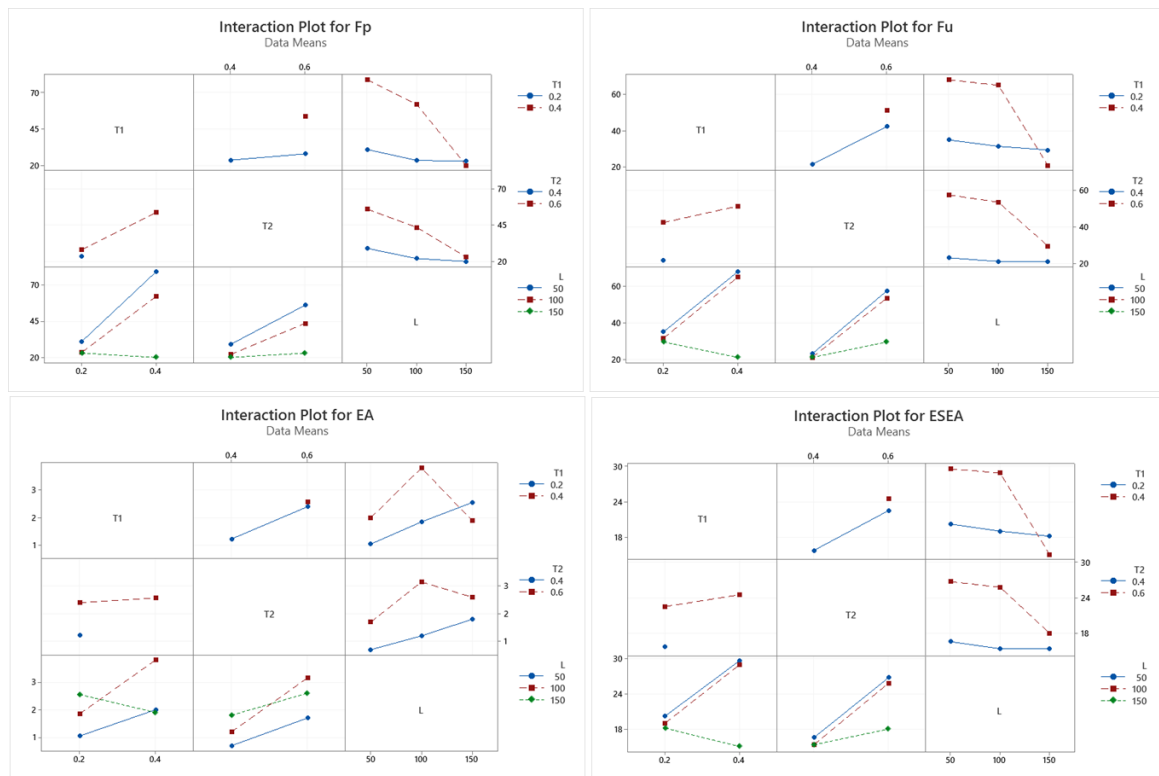
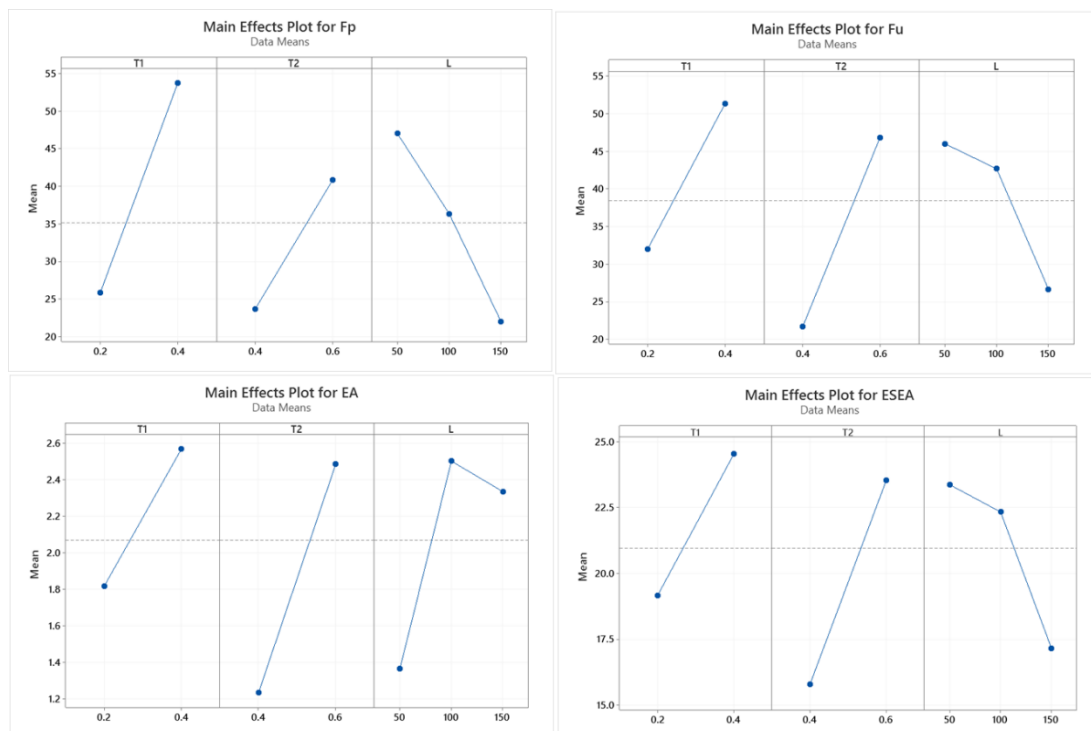**Figure 23.** Interaction plots between design parameters and performance metrics for the GT design.

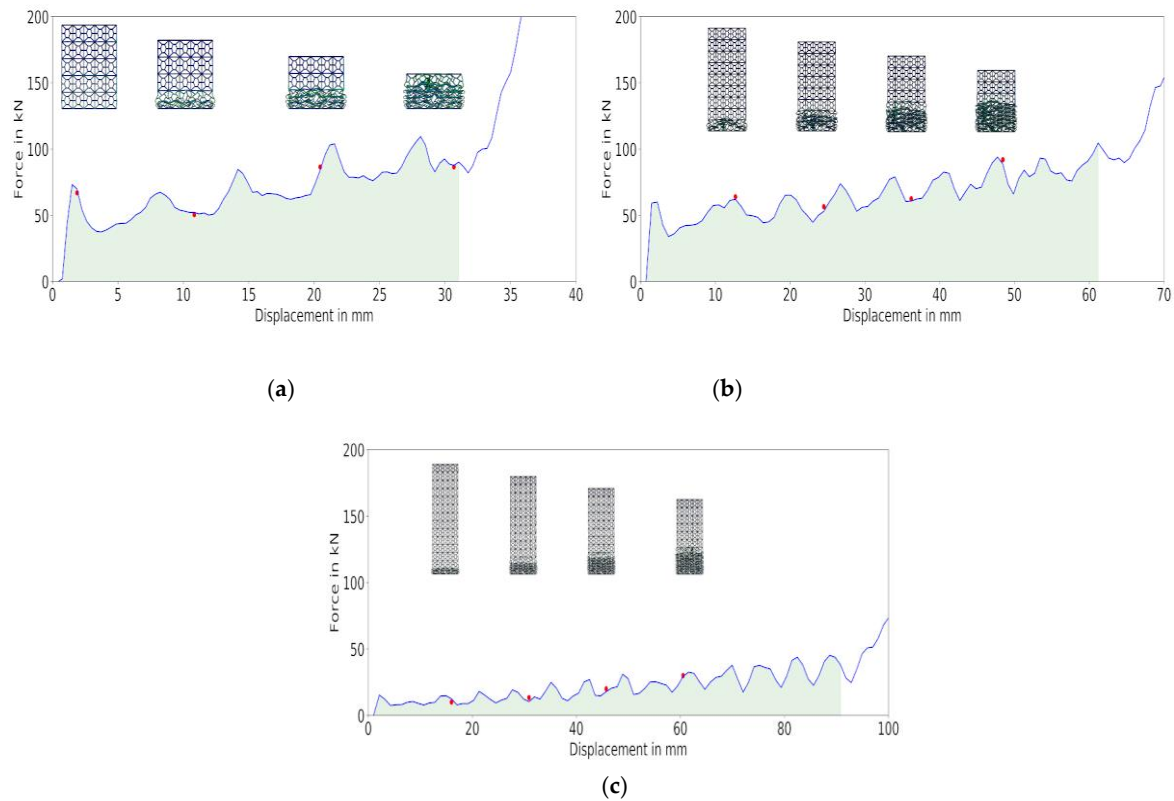**Figure 24.** Mean effect plots for each performance metric with respect to the design factors.

(**a**)

(**b**)

(**c**)

Figure 25. Example of force-displacement and deformation modes for (**a**) L = 50 mm, (**b**) L = 100 mm, (**c**) L = 150 mm. The shaded area indicates the energy absorbed before densification.

It should be noted here that in the simulations conducted in this study, the input kinetic energy was around 31 kJ as had been described in Section 3 of this paper. The maximum value of the energy absorbed by the best design reported (S9) is 8.2 kJ. Even though this is much lower than the input energy, what is important here is the specific energy absorption (E_{SEA}). For sample S9, this value is 35 kJ/kg. Which means in order to be able to absorb 31 kJ of the input energy, ideally we will require around 0.9 kg of S9 [43,48]. In terms of densification, as seen in the force displacement diagrams depicted in Figures 13, 16, 21 and 25 it is obvious that the design structures collapsed beyond the densification point, leading to a high value of forces which practically will not be safe for vehicle occupants. However, this is avoidable when a sufficient structural mass (crash element) is designed. For example, in the case of sample S9, ideally if 0.9 kg of structural mass (series configurations of several S9 design) is used, the deformation will not reach the point of densification as the input energy will be absorbed by the multiple S9 design arranged in a series configuration. Such studies as presented here are primarily investigating potential structural designs for crashworthiness application to reduce time and cost. Potential candidate designs will then have to undergo a full-scale vehicle crash test (simulation) with some optimization to achieve the desired design parameters to absorb the crash energy [49].

5. Conclusions

In this study, we have designed a novel lightweight cellular structure for electric vehicle battery protection. In designing the cellular structure, we have considered four different ways of applying the shell thickness that affect the collapse behavior and different performance metrics of the cellular structure. The four types of shell thickness include uniform thickness, strut wall thickness, gradient thickness, and alternate thickness. Among these, the uniform thickness performed the best with the highest E_{SEA} of 35 kJ/kg. We also considered the effect of the struts, walls, length, and gradient thicknesses on the performance metrics. However, these design configurations could not compete with

the performance metrics of the UT designs. This UT design has the potential to be incorporated in electric vehicles to protect the battery compartment. Being cellular structure in nature, it is expected to reduce the weight of the battery compartment without compromising the crashworthiness characteristics.

Appendix A

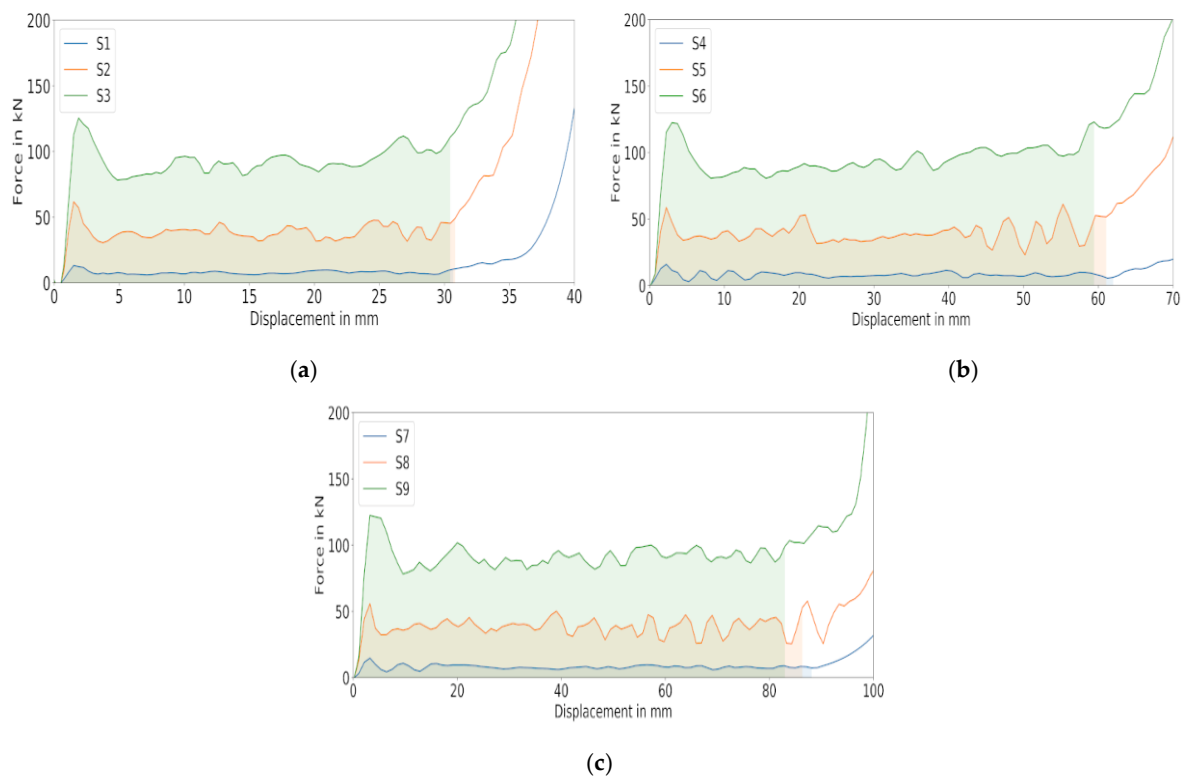**Figure A1.** (**a–c**) Force-displacement curves for UT type cellular structures.
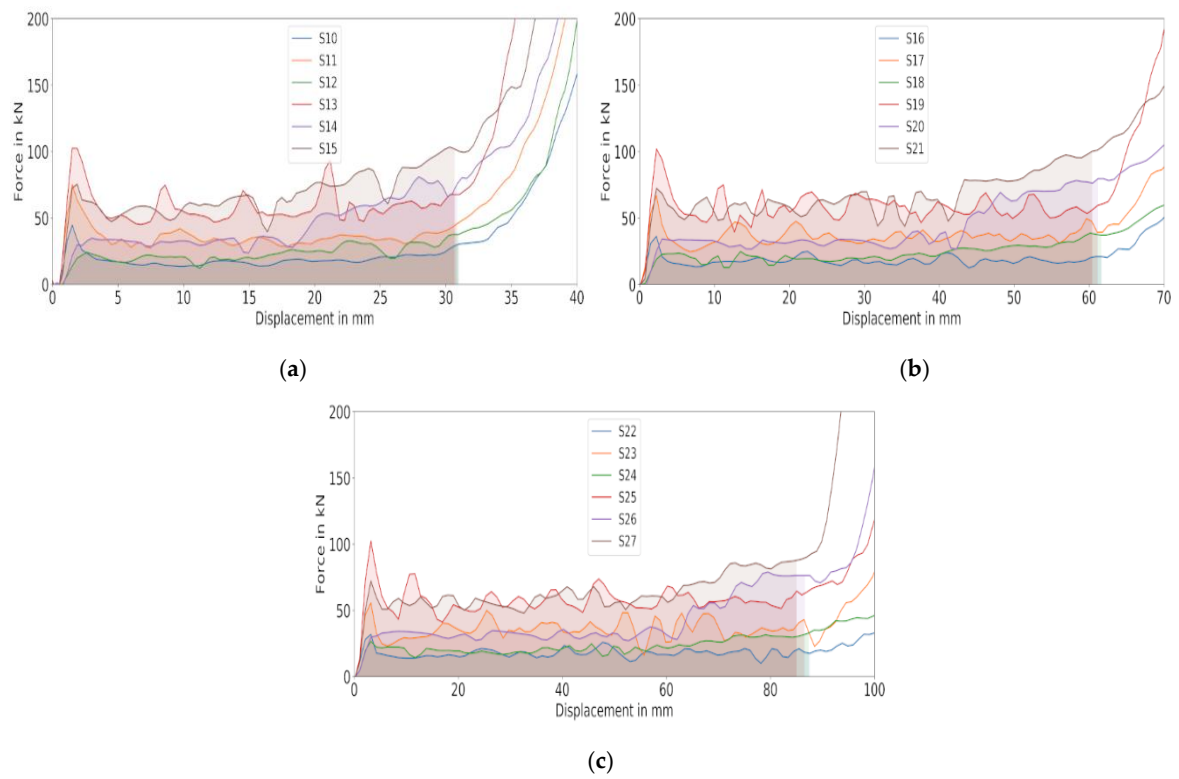
Figure A2. (**a**–**c**) Force-displacement curves for SWT type cellular structures.
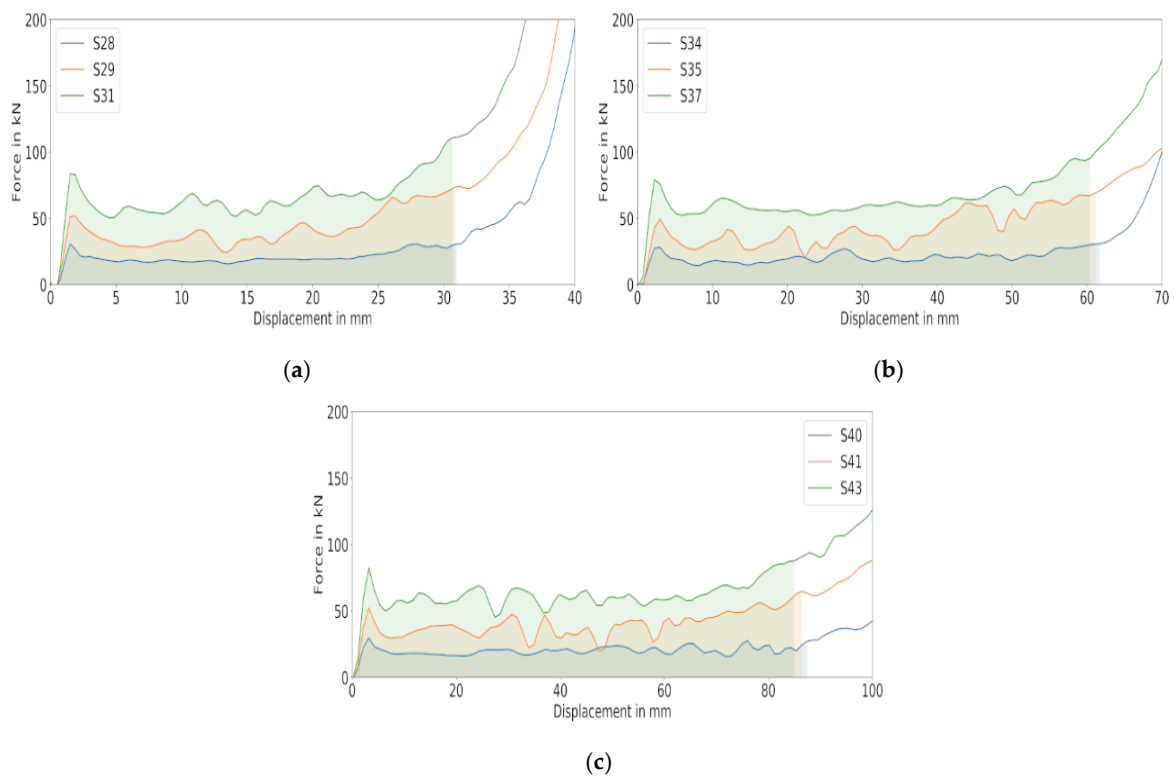

Figure A3. (**a**–**c**) Force-displacement curves for AT type cellular structures.

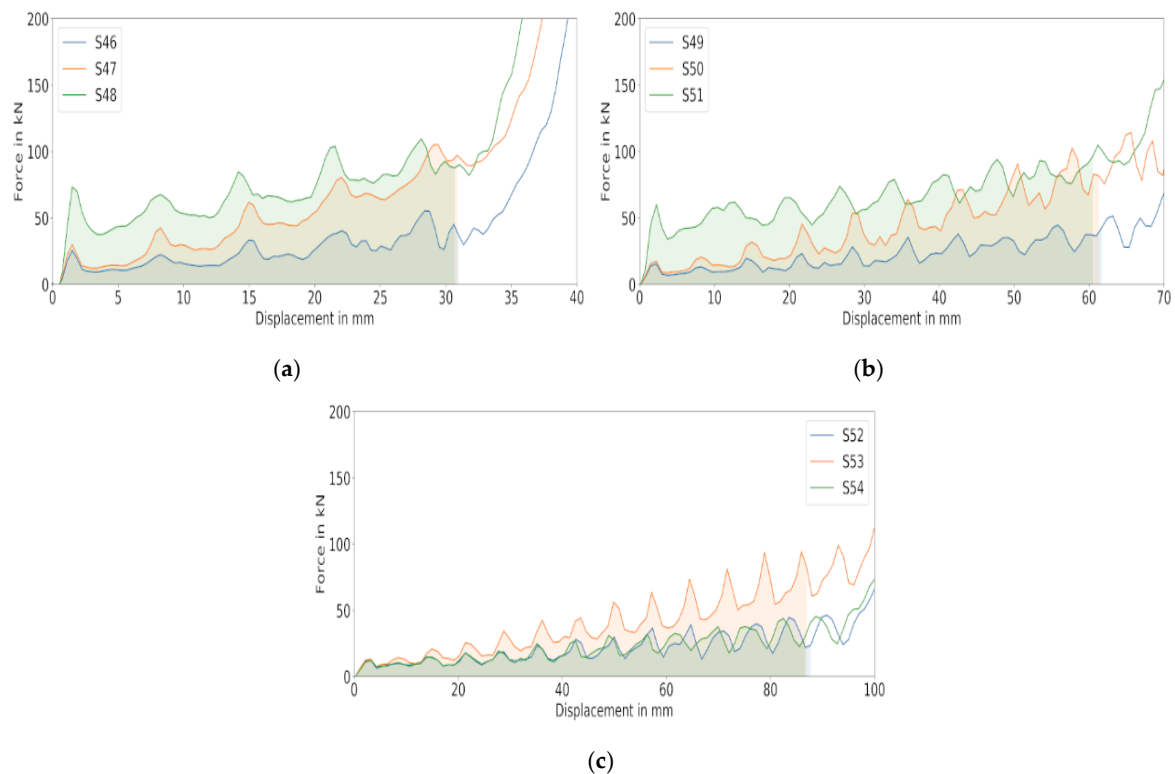**Figure A4.** (**a**–**c**) Force-displacement curves for GT type cellular structures.

References

1. Muneer, T.; Kolhe, M.L.; Doyle, A. *Electric Vehicles: Prospects and Challenges*, 1st ed.; Elsevier: Amsterdam, The Netherlands, 2017; pp. 1–91.

2. Aasness, M.A.; Odeck, J. The increase of electric vehicle usage in Norway—Incentives and adverse effects. *Eur. Transp. Res. Rev.* **2015**, *7*, 34. [CrossRef]

3. Knudsen, C.; Alister, D. Norway's electric cars zip to new record: Almost a third of all sales. *Reuters* **2019**. Available online: https://www.reuters.com/article/us-norway-autos/norways-electric-cars-zip-to-new-record-almost-a-third-of-all-sales-idUSKCN1OW0YP (accessed on 29 June 2020).

4. Hall, D.; Lutsey, N. Effects of battery manufacturing on electric vehicle life-cycle greenhouse gas emissions. *Int. Counc. Clean Transp.* **2018**. Available online: https://theicct.org/sites/default/files/publications/EV-life-cycle-GHG_ICCT-Briefing_09022018_vF.pdf (accessed on 30 March 2020).

5. Charlton, A. Longest range electric cars 2019: EVs to buy with the longest charge. *Car Mag.* **2019**. Available online: https://www.carmagazine.co.uk/electric/longest-range-electric-cars-ev/ (accessed on 29 June 2020).

6. Arbizzani, C.; de Giorgio, F.; Mastragostino, M. Battery parameters for hybrid electric vehicles. In *Advances in Battery Technologies for Electric Vehicles*, 1st ed.; Woodhead Publishing: Amsterdam, The Netherlands, 2015; pp. 3–16.

7. Mayyas, A.; Omar, M.; Hayajneh, M.; Mayyas, A.R. Vehicle's Lightweight Design vs. Electrification from Life Cycle Assessment Perspective. *J. Clean. Prod.* **2017**, *167*, 687–701. [CrossRef]

8. Lopez, L. Life, death, and spontaneous combustion—Here's why the debate about Tesla fires just got more fierce. *Bus. Insider* **2019**. Available online: https://www.businessinsider.com/why-tesla-cars-catch-on-fire-2019-4 (accessed on 29 June 2020).

9. Tesla is sued for a passenger death due to a defective battery. *Reuters* **2019**. Available online: https://www.reuters.com/article/us-tesla-crash/tesla-sued-for-passenger-death-due-to-defective-battery-idUSKCN1P228B (accessed on 29 June 2020).

10. Li, Z.; Khajepour, A.; Song, J. A comprehensive review of the key technologies for pure electric vehicles. *Energy* **2019**, *182*, 824–839. [CrossRef]

11. Tanç, B.; Arat, H.T.; Baltacıoğlu, E.; Aydın, K. Overview of the next quarter century vision of hydrogen fuel cell electric vehicles. *Int. J. Hydrog. Energy* **2019**, *44*, 10120–10128. [CrossRef]

12. Chu, Y.; Wu, Y.; Chen, J.; Zheng, S.; Wang, Z. Design of energy and materials for ammonia-based extended-range electric vehicles. *Energy Procedia* **2019**, *158*, 3064–3069. [CrossRef]

13. Kurzweil, P. Post-lithium-ion battery chemistries for hybrid electric vehicles and battery electric vehicles. In *Advances in Battery Technologies for Electric Vehicles*, 1st ed.; Woodhead Publishing: Amsterdam, The Netherlands, 2015; pp. 127–172.

14. Tu, W. Acceptability, energy consumption, and costs of electric vehicle for ride-hailing drivers in Beijing. *Appl. Energy* **2019**, *250*, 147–160. [CrossRef]

15. Matt, H. Plug-In Hybrid Electric Vehicle (PHEV) Diagram. 2009. Available online: https://commons. wikimedia.org/wiki/File:Plug-inhybridelectricvehicle(PHEV)diagram.jpg (accessed on 20 April 2020). Licensed under CC BY-SA 2.0. Available online: https://creativecommons.org/licenses/by-sa/2.0/ (accessed on 20 April 2020)..

16. Arora, S. Selection of thermal management system for modular battery packs of electric vehicles: A review of existing and emerging technologies. *J. Power Sources* **2018**, *400*, 621–640. [CrossRef]

17. Feng, X.; Ouyang, M.; Liu, X.; Lu, L.; Xia, Y.; He, X. Thermal runaway mechanism of lithium ion battery for electric vehicles: A review. *Energy Storage Mater.* **2018**, *10*, 246–267. [CrossRef]

18. Schmerler, R.; Gebken, T.; Kalka, S.; Reincke, T. Multi-functional battery housing for electric vehicles. *Light. Des. Worldw.* **2017**, *10*, 26–31. [CrossRef]

19. Mohamed, A.S.; Laban, O.; Tarlochan, F.; Al Khatib, S.E.; Matar, M.S.; Mahdi, E. Experimental analysis of additively manufactured thin-walled heat-treated circular tubes with slits using AlSi10Mg alloy by quasi-static axial crushing test. *Thin-Walled Struct.* **2019**, *138*, 404–414. [CrossRef]

20. Faris, T.; Samer, F. Design of Thin Wall Structures for Energy Absorption Applications: Design for Crash Injuries Mitigation Using Magnesium Alloy. *Int. J. Res. Eng. Technol.* **2013**, *2*, 24–36.

21. Tarlochan, F.; Hamouda, A.M.S.; Mahdi, E.; Sahari, B.B. Composite sandwich structures for crashworthiness applications. *Proc. Inst. Mech. Eng. Part L* **2007**, *221*, 121–130. [CrossRef]

22. Tarlochan, F.; Samer, F.; Hamouda, A.M.S.; Ramesh, S.; Khalid, K. Design of thin wall structures for energy absorption applications: Enhancement of crashworthiness due to axial and oblique impact forces. *Thin-Walled Struct.* **2013**, *71*, 7–17. [CrossRef]

23. Alkhatib, S.E.; Tarlochan, F.; Hashem, A.; Sassi, S. Collapse behavior of thin-walled corrugated tapered tubes. *Thin-Walled Struct.* **2018**, *122*, 510–528. [CrossRef]

24. Gibson, L.J.; Ashby, M.F. *Cellular Solids: Structure and Properties*; Cambridge University Press: Cambridge, UK, 1999.

25. Ahmad, B.; Arun, A.; Abbas, N.; Trong, N.T.; Abdul-Ghani, O. Application of Cellular Material in Crashworthiness Applications: An Overview. *Ref. Modul. Mater. Sci. Mater. Eng.* **2019**. [CrossRef]

26. Sun, G.; Wang, E.; Zhao, T.; Zheng, G.; Li, Q. Inverse identification of cell-wall material properties of closed-cell aluminum foams based upon Vickers nano-indentation tests. *Int. J. Mech. Sci.* **2020**, *176*, 105524. [CrossRef]

27. Sun, G.; Liu, T.; Fang, J.; Steven, G.P.; Li, Q. Configurational optimization of multi-cell topologies for multiple oblique loads. *Struct Multidisc Optim.* **2018**, *57*, 469–488. [CrossRef]

28. Emanoil, L.; Nima, M.; Liviu, M. The temperature and anisotropy effect on compressive behavior of cylindrical closed-cell aluminum-alloy foams. *J. Alloys Compd.* **2018**, *740*, 1172–1179.

29. Fiedler, T.; Al-Sahlani, K.; Linul, P.A.; Linul, E. Mechanical properties of A356 and ZA27 metallic syntactic foams at cryogenic temperature. *J. Alloys Compd.* **2020**, *813*, 152181. [CrossRef]

30. Zhang, S.; Chen, W.; Gao, D.; Xiao, L.; Han, L. Experimental Study on Dynamic Compression Mechanical Properties of Aluminum Honeycomb Structures. *Appl. Sci.* **2020**, *10*, 1188. [CrossRef]

31. Ashby, M.F.; Evans, A.; Fleck, N.A.; Gibson, L.J.; Hutchinson, J.W.; Wadley, H.N. Metal foams: A design guide. *Mater. Des.* **2002**, *23*, 119. [CrossRef]

32. John, B. Metal Foams: Production and Stability. *Adv. Eng. Mater.* **2006**, *8*, 781–794.

33. Degischer, H.P.; Kriszt, B. *Handbook of Cellular Metals*; Wiley-VCH: Weinheim, Germany, 2002.

34. Barletta, M.; Guarino, S.; Montanari, R.; Tagliaferri, V. Metal foams for structural applications: Design and manufacturing. *Int. J. Comput. Integr. Manuf.* **2007**, *20*, 497–504. [CrossRef]

35. Barletta, M.; Gisario, A.; Guarino, S.; Rubino, G. Production of Open Cell Aluminum Foams by Using the Dissolution and Sintering Process (DSP). *J. Manuf. Sci. Eng.* **2009**, *131*, 1–10. [CrossRef]

36. Khalid, R. Achieving Consistency and Reliability in Additive Manufacturing. *Qual. Mag.* **2018**. Available online: https://www.qualitymag.com/articles/94637-achieving-consistency-and-reliability-in-additive-manufacturing (accessed on 20 April 2020).

37. Zhang, Y.; Wu, L.; Guo, X.; Kane, S.; Deng, Y.; Jung, Y.G.; Je-Hyun, L.; Jing, Z. Additive Manufacturing of Metallic Materials: A Review. *J. Mater. Eng. Perform.* **2018**, *27*, 1–13. [CrossRef]

38. De Pasquale, G.; Luceri, F. Experimental validation of Ti6Al4V bio-inspired cellular structures from additive manufacturing processes. *Mater. Today Proc.* **2019**, *7*, 566–571. [CrossRef]

39. Hu, D.; Wang, Y.; Song, B.; Dang, L.; Zhang, Z. Energy-absorption characteristics of a bionic honeycomb tubular nested structure inspired by bamboo under axial crushing. *Compos. Part B Eng.* **2018**, *162*, 21–32. [CrossRef]

40. Ngoc, S.H.; Guoxing, L. A review of recent research on bio-inspired structures and materials for energy absorption applications. *Compos. Part B* **2020**, *181*, 107496.

41. MatWeb, Aluminum 2024-T4; 2024-T351. Available online: http://www.matweb.com/search/datasheet_print.aspx?matguid=67d8cd7c00a04ba29b618484f7ff7524 (accessed on 30 March 2020).

42. Khan, A.S.; Liu, H. Variable strain rate sensitivity in an aluminum alloy: Response and constitutive modeling. *Int. J. Plast.* **2012**, *36*, 1–14. [CrossRef]

43. Witteman, W.J. Improved Vehicle Crashworthiness Design by Control of the Energy Absorption for Different Collision Situations. Ph.D. Thesis, Eindhoven University of Technology, Eindhoven, The Netherlands, 1999; ISBN 90-386-0880-2.

44. Fornells, A.; Parera, N. Safety Protocol for Crash Tests Involving Electric and Hybrid Vehicles. *SAE Tech. Paper* **2017**. [CrossRef]

45. Gupta, S.; Abotula, S.; Shukla, A. Determination of Johnson-Cook Parameters for Cast Aluminum Alloys. *J. Eng. Mater. Technol.* **2014**. [CrossRef]

46. Li, M.; Deng, Z.Q.; Guo, H.W.; Liu, R.Q.; Ding, B.C. Optimizing crashworthiness design of square honeycomb structure. *J. Cent. South Univ.* **2014**, *21*, 912–919. [CrossRef]

47. Stanczak, M.; Fras, T.; Blanc, L.; Pawlowski, P.; Rusinek, A. Blast-induced compression of a thin-walled aluminum honeycomb structure—Experiment and modeling. *Metals* **2019**, *9*, 1350. [CrossRef]

48. Jacob, G.C.; Fellers, J.F.; Simunovic, S.; Starbuck, J.M. Energy Absorption in Polymer Composites for Automotive Crashworthiness. *J. Compos. Mater.* **2002**, *36*, 813–850. [CrossRef]

49. Khatri, N.A.; Shaikh, H.; Maher, Z.A.; Shah, A.; Ahmed, S.F. A Review on Optimization of Vehicle Frontal Crashworthiness for Passenger Safety. *Int. J. Eng. Technol.* **2018**, *7*, 1–4. [CrossRef]